

Reviving Anode Protection Layer in Na-O₂ Batteries: Failure Mechanism and Resolving Strategy

Xiaoting Lin, Yipeng Sun, Qian Sun, Jing Luo, Yang Zhao, Changtai Zhao, Xiaofei Yang, Changhong Wang, Hanyu Huo, Ruying Li, and Xueliang Sun*

Na-O₂ batteries are attractive for energy storage due to their high theoretical energy density. In order to alleviate Na dendrite formation, artificial protective coatings have been widely investigated in Na-metal batteries (NMBs). Although it can be intuitive to expect transferable Na protection methodologies from NMBs to Na-O₂ batteries, the performance of anode protection coatings in Na-O₂ batteries remains obscure, because Na-O₂ batteries undergo a unique reaction mechanism involving superoxide. Here, the effect of superoxide crossover on the polymeric Na protection layer in Na-O₂ batteries is revealed, and an effective strategy to eliminate the implications of a superoxide-sensitive protecting layer is proposed. Using polymeric alucone protected Na anode as an example, the alucone layer actually decomposes under superoxide attack and is incapable of facilitating long-term cycling of Na-O₂ batteries in sharp contrast to its stable performance in NMBs. By blocking superoxide crossover with solid-state electrolytes (SSEs), significantly improved Na-O₂ cell performance is demonstrated, recovering the Na dendrite suppressing effect of the alucone film. Benefiting from the synergistic effect of SSE and alucone layer, Na-O₂ batteries can achieve a long life of 325 cycles at 0.2 mA cm⁻². This work indicates that the stability of the Na protection layer against superoxide should be taken into serious consideration.

1. Introduction

Growing environmental concerns and continuously surging demand for energy have stimulated extensive interests in exploring advanced energy storage systems. In the past decades, the success of Li-ion batteries (LIBs) in portable electronics have greatly innovated our modern lifestyle. However, this battery system is still limited by its low energy density, and the development of next-generation electric vehicles obliges scientific and technological breakthroughs beyond LIBs. Na-O₂ batteries are appealing for their ultra-high theoretical energy density, which is six–ninefold higher than that of the conventional LIBs.^[1] Additionally, the high round-trip energy efficiency, as well as the natural abundance and low-cost of sodium


resources make Na-O₂ batteries promising for large-scale application.^[2] However, the daunting challenges of Na-O₂ batteries, such as low rechargeability and poor cycle life that relevant to the metallic Na anode, should be well addressed before the realization of practical Na-O₂ batteries.^[3]

Na dendrite growth is one of the major reasons for the premature failure of Na-O₂ batteries.^[4] The growth of Na dendrite during repetitive cycling can penetrate through the separator, causing short circuit and safety concerns.^[5] The Na dendrite can also be isolated from the bulk Na during the stripping process and becomes the “dead Na”, which is responsible for the increased interfacial resistance and fast decay of Na-O₂ cell performance. Different strategies have been proposed to facilitate the efficient use of Na metal anode, and some Na metal protection methods can be transferable from the Na-metal batteries (NMBs).^[5b,c,6] One effective approach to suppress the Na dendrite formation in Na-O₂ batteries is increasing the effective

electrode surface area to dissipate the current density.^[7] This can be realized by constructing a 3D composite electrode with reduced graphene oxide as the Na host, as reported by Luo and colleagues.^[7a] Our group have previously demonstrated that the introduction of carbon paper (CP) interlayer on Na anode also can facilitate dendrite-free Na deposition, and the reversibility and cycle life of Na-O₂ batteries can be significantly improved.^[7b] Surface engineering is another typical approach to stabilize the solid electrolyte interphase (SEI) layer and suppress Na dendrite growth.^[8] For example, Zhou and coworkers built an inorganic NaF-rich protective layer on Na anode by adding a sacrificial electrolyte additive, which can strengthen the interface to effectively inhibit the dendrite propagation in Na-O₂ batteries.^[8b]

Various polymer-based organic and inorganic-organic hybrid protection films have also been developed in NMBs, with great success in enhancing the cycling stability of metallic Na anode.^[8c,9] Although it is natural to expect the Na protection methodologies that have been already found to be profound in NMBs should also bring significant improvements of the cycling behavior of Na-O₂ batteries, there are yet few studies detailing the behavior of these Na protection (methods) in Na-O₂ batteries.^[8b] Uniquely, superoxide intermediate species dissolve in the organic electrolyte during the operation of Na-O₂ batteries. Superoxide radicals can serve as a promoter to the

Dr. X. Lin, Y. Sun, Dr. Q. Sun, J. Luo, Dr. Y. Zhao, Dr. C. Zhao, Dr. X. Yang, Dr. C. Wang, Dr. H. Huo, R. Li, Prof. X. Sun
Department of Mechanical and Materials Engineering
University of Western Ontario
London, Ontario N6A 5B9, Canada
E-mail: xsun@eng.uwo.ca

 The ORCID identification number(s) for the author(s) of this article can be found under <https://doi.org/10.1002/aenm.202003789>.

DOI: 10.1002/aenm.202003789

decomposition of organic electrolytes, polymer binders, and carbon cathodes due to its nucleophilic attacks.^[10] The critical role of Na anode protection and the importance of superoxide blockage for achieving safe and high-performance Na-O₂ batteries have been reported in our and other's previous work.^[7b,11] However, the understanding of the detrimental effect of superoxide crossing is still limited. To the best of our knowledge, the effects of superoxide crossover in Na-O₂ batteries on the Na surface protection layers, especially those prone to superoxide attacking, remain unclear.

Here, we for the first time investigate the cycling stability of a typical polymeric alucone protected Na anode in Na-O₂ batteries. This polymeric film has been demonstrated with successful Na metal anode enhancement in NMBs. Nonetheless, we will show that polymeric alucone film is vulnerable to the superoxide attack and consequently fails to suppress Na dendrites in Na-O₂ batteries. To retrieve the dendrite suppressing effect of such superoxide-sensitive coating layer on Na anode for long-life Na-O₂ batteries, we herein propose an effective approach to adopt an additional solid-state electrolyte (SSE) as a physical shield to end superoxide crossover and achieve significantly improved Na-O₂ cell performance.

2. Results and Discussion

The polymeric alucone film was deposited on fresh Na metal via molecular layer deposition (MLD), which is denoted as Na@alucone electrode. A typical alucone coating process is shown in Figure S1, Supporting Information, with alternative pulses of trimethylaluminum (TMA) and ethylene glycol (EG) at 90 °C, following our previous work with 50 MLD cycles.^[9a] The successful coating of alucone layer on Na foil was confirmed by time-of-flight secondary ion mass spectrometry (ToF-SIMS). As shown in Figure S2a,b, Supporting Information, characteristic secondary ions from alucone film, such as Al⁺, C₂Al⁺, and C₂OAl⁺ were detected with strong signals at the top surface of the sample. The depth-profiles were established by etching a selected area (400 × 300 μm) on the Na@alucone electrode with continuous ion sputtering (Figure S2c, Supporting Information). After sputtering for 200 s, the signals from alucone showed a large decrease, indicating the exposure of the underlying Na metal layer. The 3D images constructed from SIMS intensity and the etching depth show uniform spatial distribution of the alucone film on Na metal surface (Figure S2d, Supporting Information). The thickness of the alucone layer was estimated to be 20 nm based on the MLD growth rate of alucone on Na metal, which is consistent with the estimation based on SIMS sputtering rate (≈0.1 nm s⁻¹).^[9a]

The cycling stability of Na@alucone anode was evaluated in Na-O₂ batteries in the presence of superoxide radicals. **Figure 1a** shows the discharge/charge profiles of Na-O₂ cells with bare Na anode, and the charging process is interrupted by the dendrite short-circuiting. This result is consistent with the previous reports.^[3a,7b,11b] Even under the shallow cycling mode by limiting the discharge capacity to 0.2 mAh cm⁻² at 0.2 mA cm⁻², the dendrite penetration induced potential drop also can be observed from the 9th cycle (Figure 1b). As for the cell with Na@alucone anode, stable discharge plateau at

≈2.0V with the formation of micrometer-sized NaO₂ cubes as the only discharge product indicated normal electrochemistry of Na-O₂ batteries using Na@alucone anode (Figure S3, Supporting Information). However, unlike the success in NMBs,^[9a] the Na@alucone anode exhibit no obvious improvement over the bare Na anode in terms of electrochemical performance. Slight increase of discharge capacities was observed, while dendrite formation was just delayed rather than completely inhibited after introducing an alucone protective layer on Na metal (Figure 1c). As shown in Figure 1d, stable discharge/charge cycling was maintained for only 14 cycles.

The Na@alucone anode facilitated long-term cycling of NMBs,^[9a] while Na-O₂ cells with Na@alucone anode still suffered from Na dendrites induced short circuit (Figure 1c,d). The distinct stripping/plating behaviors of Na@alucone anode in NMBs and Na-O₂ cells can be possibly related to the different working chemistries of the two battery systems. To verify the effects of migrated superoxide to alucone protective layer efficacy in suppressing the dendrite growth, a hybrid solid-state (HSS) Na-O₂ battery was constructed. By replacing the porous glass fiber (GF) separator with dense NASICON-type SSE, the superoxide crossover from cathode to anode was eliminated.^[12] NASICON-type SSE was chosen in this work because of its high ionic conductivity (Figure S4, Supporting Information), wide electrochemical stability window, as well as good stability against Na metal.^[12] In addition, NASICON structures are chemically stable against oxygen and moisture, which is desirable for constructing Na-O₂ batteries.^[13] Interestingly, the constructed HSS Na-O₂ batteries delivered high discharge capacities of 5.33 and 4.51 mAh cm⁻² at 0.1 and 0.2 mA cm⁻², respectively (Figure 1e). The discharge capacities were much higher than that of the cells using GF separator and Na@alucone anode in Figure 1c. Since the air electrode of two cell configurations was the same, the lower discharge capacity of Na-O₂ batteries with GF was attributed to the corrosion of Na@alucone anode by superoxide crossover.^[12]

Interestingly, in addition to the significant increase in discharge capacities, the HSS Na-O₂ cells with Na@alucone anode can be fully recharged without dendrite-induced short circuit, and the corresponding Coulombic efficiencies are as high as 95.10 and 90.14% at 0.1 and 0.2 mA cm⁻², respectively. Additionally, significantly improved cycling stability of HSS Na-O₂ cell can be achieved with a long cycle life of over 95 cycles, as shown in Figure 1f-h. It is believed that the SSEs are more effective in inhibiting dendrite penetration compared with porous GF separators. However, long-term plating/stripping of dendrite-free Na anode with the pure SSE pellet is still a challenge since the Na dendrite tends to grow through grain boundaries and interconnected pores in the SSE.^[12,14] As shown in Figure S5, Supporting Information, HSS Na-O₂ cells based on SSE and bare Na anode still suffered from the short-circuiting issue and failed to cycle beyond 40 cycles under the same experimental conditions. The optical images of the cycled SSE clearly display "dark spots" on the surface, which can be reasonably assigned as Na dendrite and were found to penetrate across the SSE pellet after cell failure (Figure S6, Supporting Information). The employment of SSE partially contributed to the long-term cycling of HSS Na-O₂ batteries in Figure 1f, the integration of SSE with Na@alucone anode was crucial to

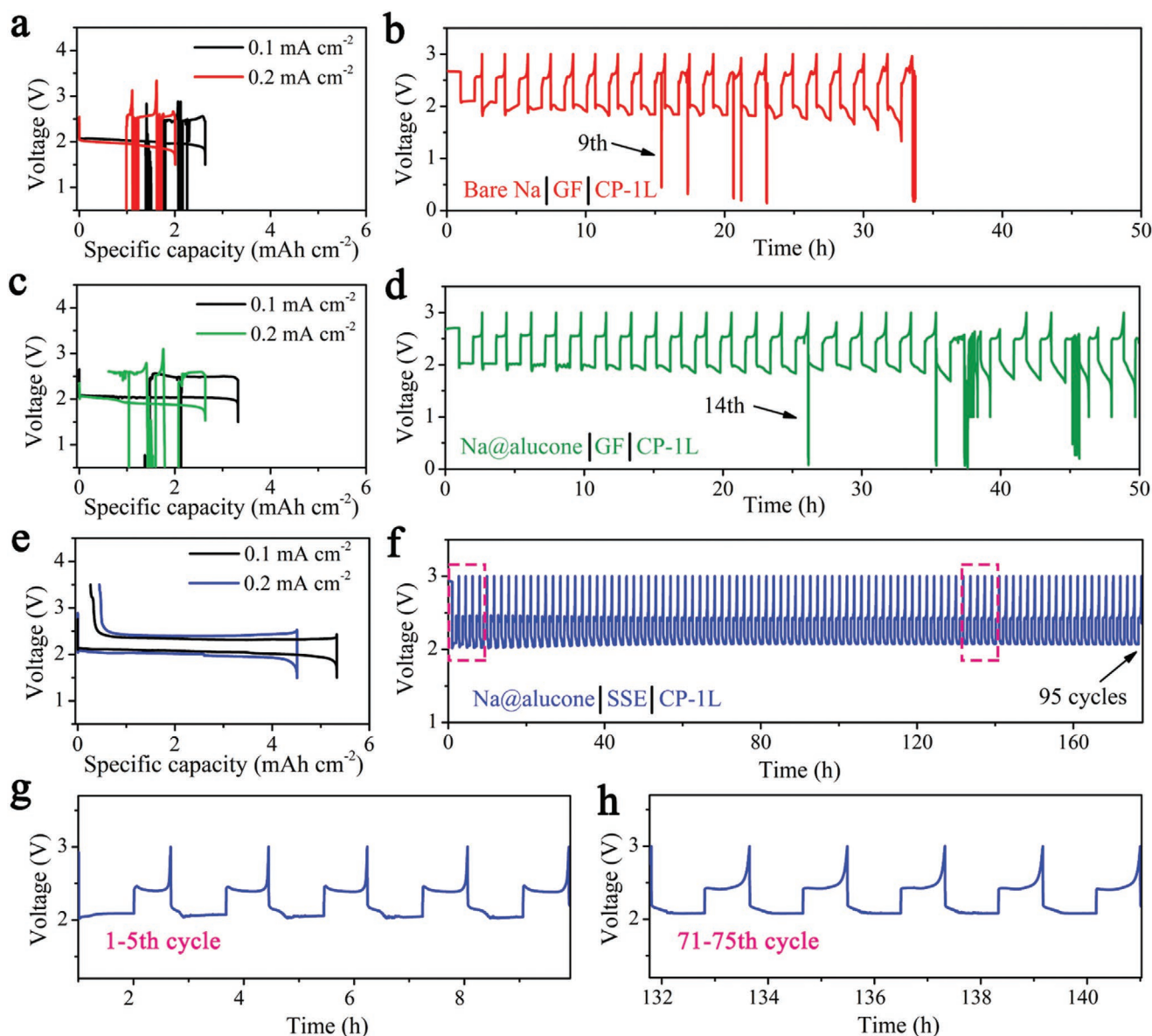


Figure 1. The discharge/charge profiles and cycling performance of Na-O₂ cells with different configurations: a,b) Na-O₂ cells with GF separator and bare Na anode, c,d) Na-O₂ cells with GF separator and Na@alucone anode, and e,f) HSS Na-O₂ cells with SSE and Na@alucone anode. g,h) Enlarged discharge/charge profiles of the HSS Na-O₂ cell at selected cycles. The sudden voltage drops in Figure 1a–d are caused by a short circuit from Na dendrite growth and penetration.

simultaneously address short circuit and anode degradation. It is worth noting that the slightly higher discharge/charge overpotential in the initial cycles may be attributed to the sodiation of alucone layer with the formation of a new SEI layer. Benefiting from the formation of this new protective SEI layer, flat voltage profiles during both discharge and charge can be well retained during the subsequent cycles without an obvious increase in discharge/charge overpotentials.

Collecting the Na@alucone anodes from the Na-O₂ batteries with GF or SSE after cycling, their different morphologies gave hints to their distinct electrochemical behaviors. Both Na-O₂ cells were cycled at 0.2 mA cm⁻² with a cutoff capacity of 0.2 mAh cm⁻². From the SEM images shown in Figure S7,

Supporting Information, the uncycled Na@alucone anode exhibited a clean and relatively smooth surface. After cycling in the Na-O₂ cell with a GF separator, the Na@alucone anode shows a cracked surface with inhomogeneous Na deposition on the bulk Na electrode (Figure S8, Supporting Information). At the same time, Na dendrites of approximately 10–20 μm can be clearly observed on the cycled Na@alucone electrode (Figure 2a,b). The corresponding cross-sectional view clearly shows that the top surface of the original bulk Na has transformed to the high-surface-area porous structure (Figure 2c). The formation of porous layer indicates the destruction of protective alucone film on the Na metal anode. This porous layer was permeable to superoxide that corrodes the Na anode, and

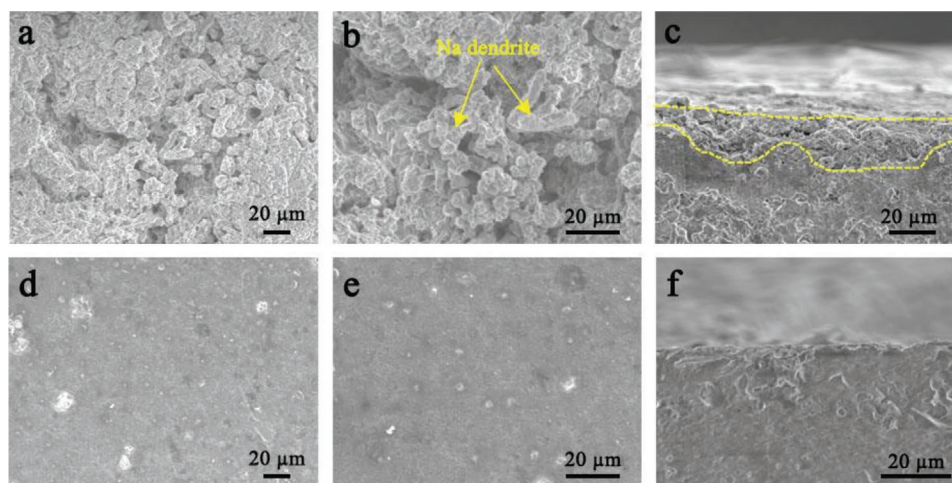


Figure 2. a,b) Top-view and c) cross-sectional view SEM images of the Na@alucone anode obtained from cycled Na-O₂ cell with GF separator; the distance between two dotted yellow lines in (c) shows the thickness of porous Na. d,e) Top-view and f) cross-sectional view SEM images of the Na@alucone anode obtained from cycled Na-O₂ cell with SSE.

thus continuous electrolyte decomposition and active Na consumption were unavoidable. The optical and SEM images of the GF separator are shown in Figure S9, Supporting Information, the presence of dendritic spots on the GF surface on the side facing the CP cathode further verified the dendrite penetration issue. In sharp contrast, as shown in Figure 2d,e and Figure S10, Supporting Information, a relatively smooth surface without dendritic Na or unfavorable porous layer can be observed on the cycled Na@alucone electrode after introducing SSE. The unchanged SSE surface had no sign of Na dendrites growth (Figure S11, Supporting Information). Meanwhile, the cross-sectional view of the Na@alucone displayed a negligible gap between plated Na and bulk Na (Figure 2f). The results indicated that the shielding effect of SSE against superoxide crossover restores the dendrite suppressing function of alucone on the Na metal anode.

ToF-SIMS analyses were conducted on the cycled Na@alucone anodes with or without exposure to superoxide crossover to further understand the interfacial changes of the Na@alucone anodes. It should be noted that electrolyte decomposition cannot be avoided on the anode surface with the formation of various organic and inorganic species including Na₂CO₃, NaF, NaOH, RONa, ROONa, et al.^[12] To have a clear picture of the changes of alucone film, only the variation of Al-containing secondary ions that are exclusively generated from the alucone film were analyzed. Figure 3a illustrates the ToF-SIMS chemical mappings of secondary ions of interest on the Na@alucone electrode after cycling in the presence of superoxide crossover. Surprisingly, although the secondary ion fragments from alucone still can be detected on the surface of Na@alucone anode, the intensity of those species significantly decreased after cycling. For example, compared with the pristine sample in Figure S2, Supporting Information, the signals of C₂Al⁻ decreased dramatically from 200 to 40 counts, while the signals of Al⁻ and C₂OAl⁻ become negligible. From Figure 3b,c, the alucone protective layer was not visible on the electrode surface, which suggested the breakdown of the alucone film during cycling. However, the sputtering depth should

not be mistaken as the thickness of the SEI layer. Considering serious electrolyte decomposition on the electrode surface due to malfunction of the alucone layer in protecting Na anode when exposed to superoxide crossover, a stable SEI layer cannot be formed. As shown in Figure S12a, Supporting Information, the alucone film can be completely destroyed and lose its protective effect after 5 cycles, resulting in a significant increase in internal cell resistance due to the accumulation of parasitic products on the anode surface.

In contrast, after cycling in the absence of superoxide crossover, the Na@alucone anode still showed strong signals of secondary ions from alucone (C₂Al⁻, COAl⁻, and C₂OAl⁻) on the outermost surface (Figure 3d-f). By consecutive sputtering for 500s, an area with a depth of ≈50 nm was removed to obtain the depth profiles and 3D view images of various fragments (Figure 3e,f). The signals of secondary ions from alucone remain distinct from the top surface to the interior of the electrode, despite the slight decrease in intensity compared with pristine sample, suggesting preservation of the robust alucone film after cycling. Notably, the sodiated alucone layer has a thickness of ≈25 nm (considering the sputtering rate of 0.1 nm s⁻¹), which is thicker than the pristine alucone film before cycling. This observation suggests a newly formed SEI layer on the Na@alucone electrode during the cycling process. Moreover, little change in the overall cell impedance can be observed after the surface of Na@alucone anode was completely stabilized by the 5th cycle (Figure S12b, Supporting Information), which further demonstrates the effectiveness of alucone layer to stabilize the Na anode after eliminating the superoxide crossover effect.

Although the electrochemical reversibility of Na@alucone anode in the Na-O₂ batteries can be significantly improved by incorporating SSE, the chemical stability of SSE against the highly reactive NaO₂ also cannot be neglected. As the SSE was in direct contact with the CP cathode, and the accumulation of NaO₂ cubes on the SSE surface is inevitable due to the growth of NaO₂ through solution-mediated mechanism.^[12] The possible reactions between SSE and NaO₂ not only can

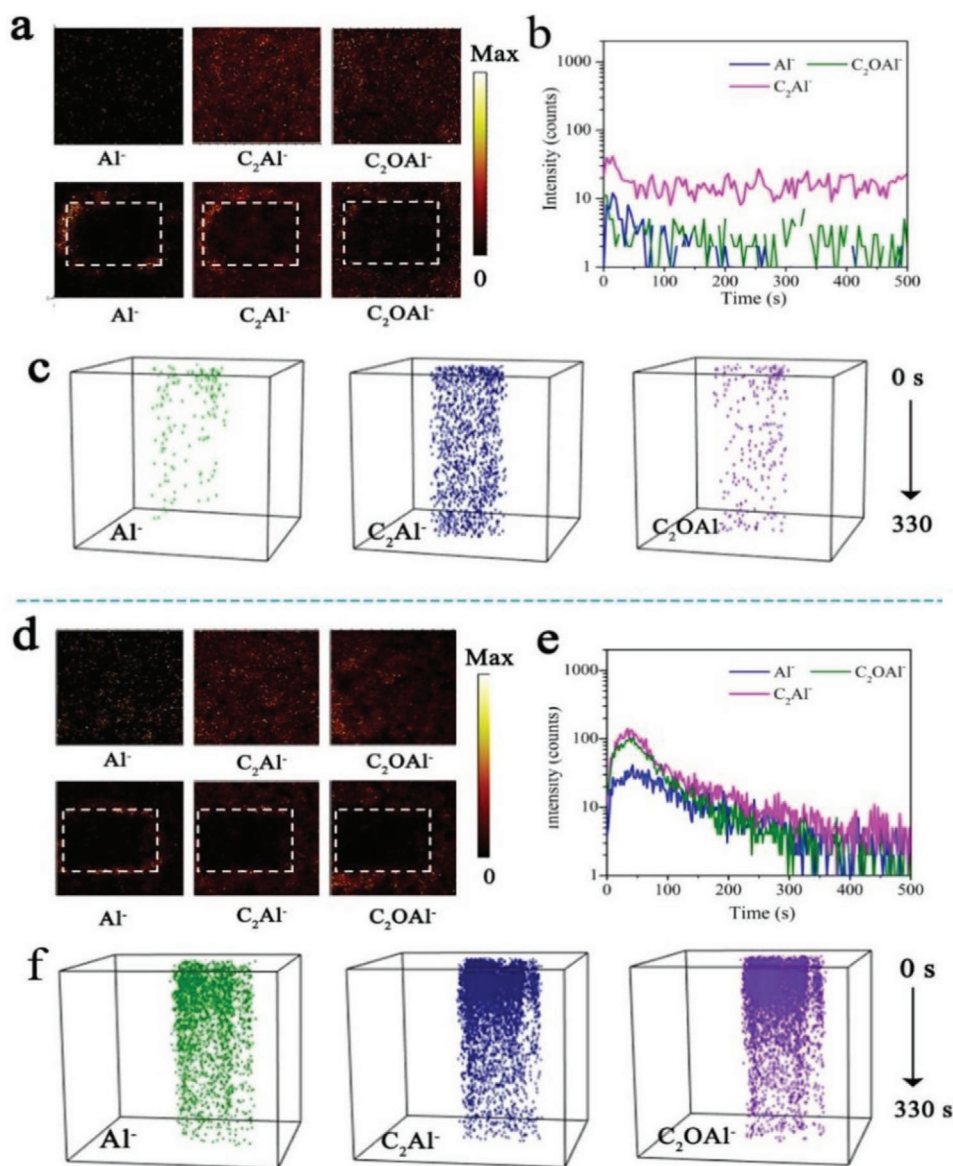


Figure 3. a,b) TOF-SIMS depth profiles and chemical ion images of the Al^- , C_2Al^- , and C_2OAl^- species for the cycled Na@alucone anode obtained from Na- O_2 cell with GF separator. c) The corresponding 3D view images of the variation of SIMS intensity with the etching depth. d,e) TOF-SIMS depth profiles and chemical ion images of the Al^- , C_2Al^- , and C_2OAl^- species for the cycled Na@alucone anode obtained from Na- O_2 cell with SSE. f) The corresponding 3D view images of the variation of SIMS intensity with the etching depth.

decrease the reversible charge capacity due to the consumption of NaO_2 , but also result in the increase of internal cell resistance as a result of side product formation. Here, we employ in situ Raman imaging technique to monitor the chemical changes of NaO_2 cube when in contact with the SSE. The SSE was collected from a discharged HSS Na- O_2 cell. The distribution of NaO_2 cubes on the SSE can be clearly observed via Raman and SEM microscope (Figure S13, Supporting Information). As shown in Figure S14, Supporting Information, a NaO_2 cube was linearly scanned, and the Raman spectra were collected in an area of $15 \mu\text{m} \times 15 \mu\text{m}$ for 15 points in each X and Y directions. Figure 4a,b shows the Raman spectra collected from two vertical liner scans on the NaO_2 cube after a period of 24 h. The characteristic Raman peak located at 1156 cm^{-1} was related to

the O–O stretching mode in NaO_2 , and weak Raman peak at 1136 cm^{-1} corresponded to $\text{Na}_2\text{O}_2 \cdot 2\text{H}_2\text{O}$. The obtained spectra were converted into 2D mapping images using the chemical maps at frequencies of 1136 and 1156 cm^{-1} (Figure 4c). As clearly evidenced in Figure 4c, the intensity of the NaO_2 chemical maps showed a slightly decreasing trend over time, along with a slight increase in $\text{Na}_2\text{O}_2 \cdot 2\text{H}_2\text{O}$ intensity. This phenomenon can be attributed to the transformation of NaO_2 to $\text{Na}_2\text{O}_2 \cdot 2\text{H}_2\text{O}$ in the presence of residual electrolyte solvent or air leakage of the Raman cell.^[15] However, it is notable that the absence of other obvious side products (even after 168 h) and the preservation of the original shape of NaO_2 particle again verified the excellent chemical stability of NaO_2 in contact with NASICON-type SSE (Figures S15,S16, Supporting Information).

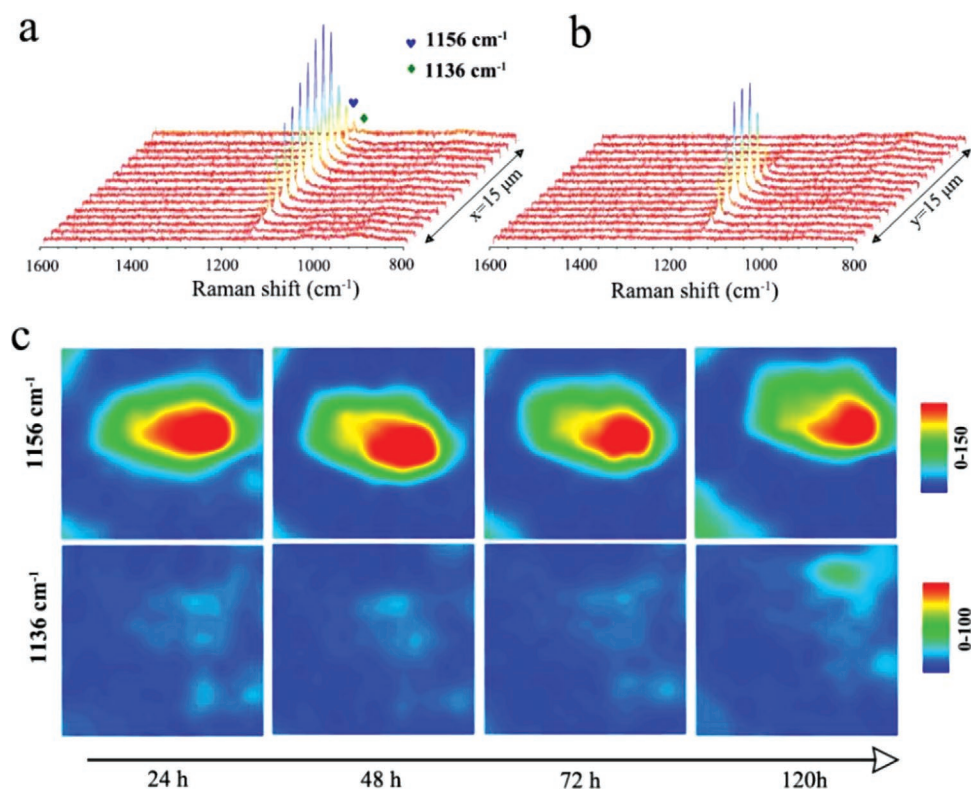


Figure 4. a,b) Raman spectra recorded over a linear scan on a typical NaO₂ cube after resting for 24 h. c) chemical maps at various frequencies reproduced from Raman spectra recorded from a NaO₂ cube on the SSE at different time intervals.

After addressing the anode issues and ruling out the possible effects of SSE, the limited cycle life of HSS Na-O₂ cell in Figure 1f may indicate a degradation effect related to the cathode.^[12] Therefore, HSS Na-O₂ cells with extra cathode loading were assembled in order to extend the Na-O₂ cell lifetime, and at the same time, to investigate the durability of Na@alucone anode during the long-term cycling process. Here, extra cathode loading was realized by simply increasing the number of CP cathode, and the cathodes with 2, 3, 4, and 5 CP are named as CP-2L, CP-3L, CP-4L, and CP-5L, respectively. The electrochemical performance of HSS Na-O₂ batteries with different cathodes was investigated at 0.2 mA cm⁻² with a cutoff capacity of 0.2 mAh cm⁻². It can be seen from Figure 5 and Figure S17, Supporting Information, that the cycle life of HSS Na-O₂ cells increased with increasing the cathode loading. The HSS Na-O₂ cells with CP-2L, CP-3L, and CP-4L cathodes exhibited stable cycling for over 175, 238, and 292 cycles, respectively. When the Na@alucone anode was coupled with CP-5L cathode in the HSS Na-O₂ cell, the cell delivered highly stable discharge/charge performance for over 325 cycles (Figure 5b–e), which was almost 3.4 times longer lifetime than that of the CP-1L cathode in Figure 1f.

The long cycle life of the HSS Na-O₂ cell with CP-5L cathode was a reflection of good stripping/plating stability of Na@alucone anode after integrating with SSE (~565 h). The increase of cathode loading was accompanied by an increase in the number of active sites for electrochemical reactions, which contributed to the enhancement of cell life under the shallow cycling mode. However, the more active sites and longer cycling

time, the greater chance of O₂⁻ attack occurrence. Additionally, the parasitic reactions involving NaO₂, ¹O₂, and electrolyte may induce the degradation of air electrodes.^[4a,16] Coverage of active sites by the insulating side products thus results in the decrease of Coulombic efficiency along with cycling (Figure 5f). All these factors contributed to the nonlinear correlation between the cycle life of HSS Na-O₂ batteries and the number of layers of CP cathode. Another important aspect to note is that the cathode thickness increased with increasing the CP layers. Therefore, the increase of Na⁺/O₂⁻ diffusion distance and the diffusion kinetic limits of O₂ in the organic electrolyte explained the slight increase in discharge/charge overpotential of the cell using CP-5L cathode, compared with that of the cell with CP-3L cathode (Figure S19 Supporting Information).

To further verify the universality of the failure mechanism of polymeric thin-film protected Na metal anode in Na-O₂ batteries, the electrochemical behavior of Na-O₂ cells using other type of organic protective layer (polyurea) coated Na anode (Na@polyurea) was investigated as an extra example. As highly consistent with the results of Na@alucone, the Na@polyurea anode in Na-O₂ cells showed minimal improvement over bare Na anode when using GF separator (Figure S19 Supporting Information). The Na-O₂ cell with Na@polyurea anode demonstrated significant improvement in cycling stability when SSE was used to eliminate the superoxide crossover, as shown in Figure S20 Supporting Information. Those results are identical to that of the cells using Na@alucone anode in Figure 1, indicating that the corrosion of polymeric Na protection film under superoxide attacking can be common and should be highly

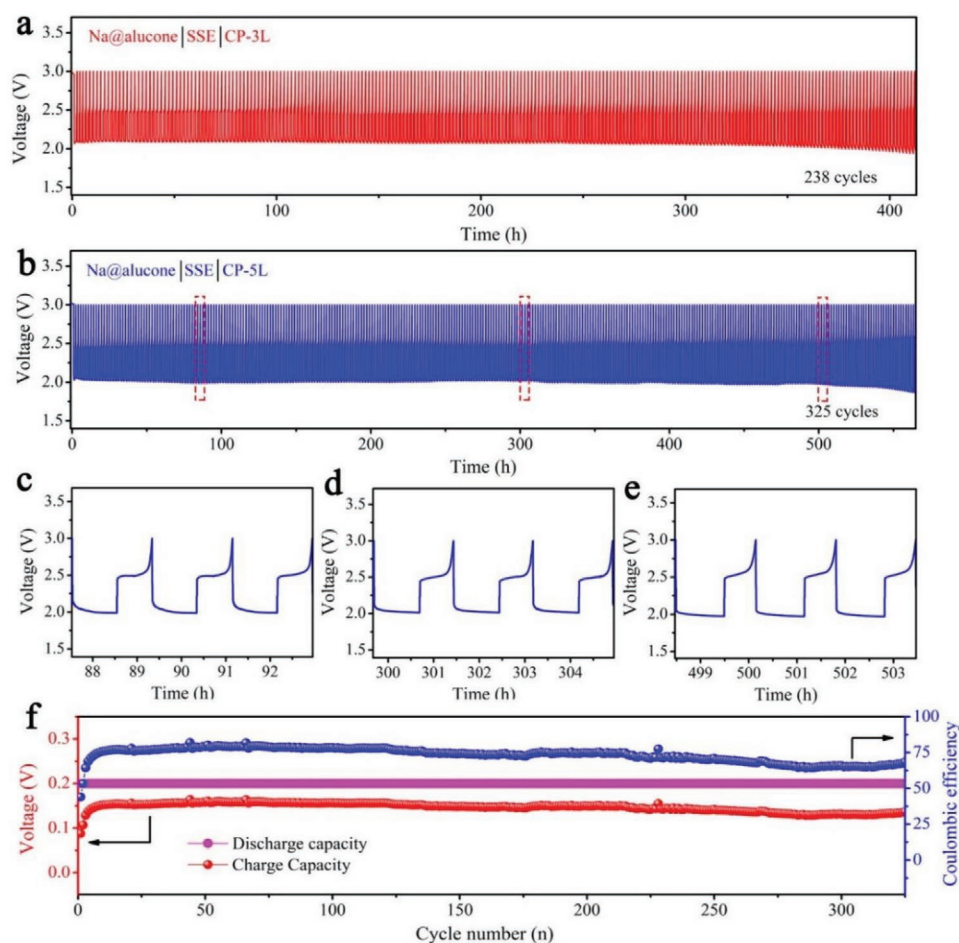


Figure 5. Cycling performance of HSS Na-O₂ cells with a) CP-3L cathode and b) CP-5L cathode; c–e) selected discharge/charge profiles of HSS Na-O₂ cell with CP-5L cathode; f) cycling performance and Coulombic efficiency of HSS Na-O₂ cell with CP-5L cathode.

aware of. Recently, researchers have verified the generation of reactive ¹O₂ in Na-O₂ batteries, which is partially responsible for the parasitic chemistry on the cathode.^[17] Except for superoxide, ¹O₂ may also migrate to the anode side and affect the cycling stability of the polymeric Na protective layer. Fortunately, the introduction of the SSE membrane can successfully block the ¹O₂ crossing. The possible effect of ¹O₂ on the anode, as well as the underlying working mechanism will be studied in our future research.

Overall, the schematic diagram of Na stripping/plating behaviors in different Na-O₂ cell configurations are illustrated in **Figure 6**. For Na-O₂ batteries, the vulnerability of polymeric protective films to superoxide should be taken into serious consideration for the Na metal anode. Insufficient Na anode protection will lead to continuous corrosion of the Na metal anode and the growth of Na dendrite. The Na degradation issue in Na-O₂ batteries is much more complicated than that in NMBs. The dissolved superoxide radicals are an aggressive species, which prone to attack electrophilic sites and induce various side reactions in Na-O₂ batteries.^[11a,15c,18] Thus, the chemical/electrochemical reduction of organic electrolyte on anode can be further aggravated in the presence of superoxide crossover, and the build-up of parasitic products on the Na anode could

result in blockage of the Na⁺ migration and soaring internal resistance.^[12] Therefore, except for the Na-O₂ battery system, the properties of metal protective layer in other batteries that involve the solution redox, such as Li-O₂, Li-S, and Na-S, may also need taken special consideration.

3. Conclusion

In summary, we have for the first time investigated the effect of superoxide crossover on the protection layer of Na metal anode and correlation to the electrochemical performance of Na-O₂ batteries. The unique superoxide ions dissolution in electrolytes plays a critical role in the electrochemical behavior of Na-O₂ batteries. Taking a typical polymeric protective layer on Na anode as an example, we found that the alucone layer suffers from decomposition under attacks of reactive superoxide radical. After eliminating the superoxide crossover effect towards Na@alucone anode with a chemical-stable SSE layer, the polymeric alucone coating retrieved its Na dendrite suppressing effect and maintained a high reversible charge capacity for Na-O₂ batteries. In addition, the cycle life of Na-O₂ cells can be significantly improved with extra cathode loading, which

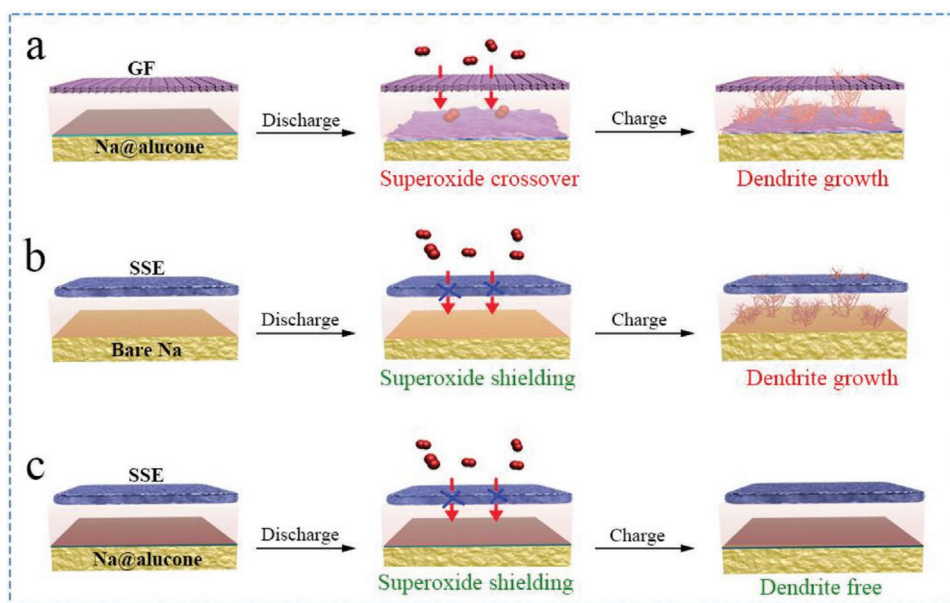


Figure 6. Schematic illustration of Na stripping/plating behaviors in Na-O₂ batteries with different configurations.

guaranteed sufficient active sites for reversible reactions. The synergistic combination of Na@alucone anode, SSE, and efficient cathode contributed to a high-performance rechargeable HSS Na-O₂ battery. Long cycle life of 325 cycles at 0.2 mA cm⁻² with a limited capacity of 0.2 mAh cm⁻² was demonstrated. The stability of Na protection layer and the issues involving the high reactive superoxide radicals should be considered seriously in Na-O₂ batteries. It is believed that our results provide important guidance for improving the cycling stability of Na anode, as well as the realization of next-generation high energy density Na-O₂ batteries.

4. Experimental Section

Synthesis of the Solid-State Electrolyte: The NASICON-type Na_{3.25}Zr₂Si_{2.25}P_{0.75}O₁₂ SSE was synthesized by a sol-gel method. Stoichiometric amounts of tetraethyl orthosilicate (Si(OC₂H₅)₄, Sigma-Aldrich, 98%) and Zirconium (IV) propoxide solution (Zr(OC₂H₅)₄, Sigma-Aldrich, 99.99%) were sequentially dissolved in ethanol at 67 °C. Then, 10 mL acetic acid and 2 mL deionized water were added dropwise. The resultant mixture was vigorously stirred at 67 °C for overnight. After that, the sodium nitrate (NaNO₃, Sigma-Aldrich, ≥99.0%) and ammonium dihydrogen phosphate (NH₄H₂PO₄, Sigma-Aldrich, 99.9%) were dissolved in deionized water separately and subsequently added into the previous solution. Next, the solution was continuously stirred and slowly dried at 67 °C to produce the gel precursor, which was heated at 500 °C for 1 h in air atmosphere to remove the organics residues. The resulting powder was first calcined in air at 500 °C for 2 h and then 1050 °C for 10 h to get the Na_{3.25}Zr₂Si_{2.25}P_{0.75}O₁₂ powders. The calcined powder was grounded and pressed into pellets (diameter of 1.3 cm and thickness of 0.1 cm) with a hydraulic press, and then sintered at 1305 °C for 12 h. Highly crystalline SSE pellets with a diameter between 1.12–1.14 cm and a thickness of around 0.09 cm can be obtained after sintering. The ionic conductivity of the as-prepared SSE pellet is 1.36 × 10⁻³ S cm⁻¹ at room temperature, with a relative density of 94.83% measured via Archimedes method.

Protected Na Anode Preparation: Fresh Na foils with a diameter of 3/8 inch were prepared in the argon-filled glovebox using a homemade

press machine. MLD of Alucone coatings on Na foil was conducted in a Gemstar-8 ALD system (Arradiance, USA), which was directly connected with the argon-filled glove box. Alucone was directly deposited on the as-prepared foil at 90 °C by TMA and EG as precursors. The MLD process used as 0.01s/40s/0.01s/70s TMA pulse/purge/EG pulse/purge sequence. The MLD-polyurea was performed on fresh Na foil by alternatively introducing ethylenediamine (ED) and phenylene diisocyanate (PDIC) as the precursors at 90 °C. A complete MLD polyurea cycle was described as ED pulse/purge/PDIC pulse/purge for period of 0.1s/30s/1s/50s.

Materials: The carbon paper (CP, H23, thickness of 210 μm), purchased from Fuel Cell Store, was utilized as the air electrodes in the Na-O₂ cells after drying under vacuum at 100 °C for 24 h. Diethylene glycol dimethyl ether (DEGDME, reagent grade ≥98%, Aldrich) was dried using freshly activated molecular sieves (4 Å, Aldrich) for at least one month. NaSO₃CF₃ (Aldrich) was dried in a vacuum at 80 °C for 1 week before use.

Electrochemical Measurement: The electrochemical performance of Na-O₂ batteries was evaluated with Swagelok-type cells. The liquid-based Na-O₂ batteries were assembled with Na foil as the anode, GF separator, CP cathode, and ether-based electrolyte. The electrolyte was 1 M NaSO₃CF₃ dissolved in DEGDME. The diameter of CP cathode was 0.9525 cm. In this work, an excess amount of Na (Na foil with a diameter of 0.9525 cm and a thickness of 0.06 cm) was used for Na-O₂ cell assembly in order to eliminate the influence of the Na amount as a limiting factor for the Na-O₂ cell performance. The Na-O₂ cells were operated under static O₂ with a pressure of 1.0 atm in a homemade testing box (≈432 cm³). Each cell was stabilized for 1 h at room temperature before electrochemical tests. The galvanostatic discharge-charge tests were carried out using Arbin BT-2000 battery testing system at room temperature. The electrolyte preparation and battery assembly were carried out in an argon-filled glovebox with oxygen and moisture levels below 0.1 ppm. Electrochemical impedance spectroscopy (EIS) measurements were carried out with multi potentiostats (VMP3, Biologic).

Characterization: The X-ray powder diffraction (XRD) patterns were collected using the Bruker D8 X-ray diffractometer equipped with Cu-Kα (λ = 1.5406 Å) radiation. The morphology of the cathodes was characterized by Hitachi S-4800 field emission scanning electron microscope (FE-SEM) at an acceleration voltage of 5 kV. The morphological studies of the GF and Na@alucone anode were

performed using a Hitachi 3400N environmental SEM. The Raman spectra were collected on a HORIBA Scientific LabRAM Raman spectrometer equipped with a 532.03 nm laser. The ToF-SIMS measurements were conducted using an ION-TOF (GmbH, Germany) ToF-SIMS IV with a bismuth liquid metal ion source. In this study, the disassembly of the Na-O₂ batteries was carried out in an argon-filled glovebox. The discharged cathodes and cycled anode were washed with DEGME to remove any residual NaSO₃CF₃ salt and dried thoroughly in a vacuum chamber before SEM, XRD, and Raman measurements. The specimens were sealed in a leak-tight homemade sample holder to prevent exposure to air during analyses of XRD and Raman.

Supporting Information

Supporting Information is available from the Wiley Online Library or from the author.

Acknowledgements

This research was supported by the National Sciences and Engineering Research Council of Canada, Canada Research Chair Program, Canada Foundation for Innovation, Ontario Research Fund, and the University of Western Ontario. X.T.L. was supported by the China Scholarship Council.

Conflict of Interest

The authors declare no conflict of interest.

Data Availability Statement

The data that support the findings of this study are available from the corresponding author upon reasonable request.

Keywords

Na dendrites, Na-O₂ batteries, polymeric Na-protection layers, solid-state electrolyte, superoxide crossover

Received: December 8, 2020

Revised: January 17, 2021

Published online:

- [1] a) P. Hartmann, C. L. Bender, M. Vračar, A. K. Dürr, A. Garsuch, J. Janek, P. Adelhelm, *Nat. Mater.* **2013**, *12*, 228; b) H. Yadegari, X. Sun, *Acc. Chem. Res.* **2018**, *51*, 1532; c) X. Bi, R. Wang, K. Amine, J. Lu, *Small Methods* **2019**, *3*, 1800247.
- [2] a) H. Yadegari, Q. Sun, X. Sun, *Adv. Mater.* **2016**, *28*, 7065; b) S. K. Das, S. Lau, L. A. Archer, *J. Mater. Chem. A* **2014**, *2*, 12623.
- [3] a) L. Medenbach, C. L. Bender, R. Haas, B. Mogwitz, C. Pompe, P. Adelhelm, D. Schröder, J. Janek, *Energy Technol.* **2017**, *5*, 2265; b) J.-l. Ma, F.-l. Meng, Y. Yu, D.-p. Liu, J.-m. Yan, Y. Zhang, X.-b. Zhang, Q. Jiang, *Nat. Chem.* **2019**, *11*, 64; c) J. L. Ma, Y. B. Yin, T. Liu, X. B. Zhang, J. M. Yan, Q. Jiang, *Adv. Funct. Mater.* **2018**, *28*, 1703931; d) H. Yang, J. Sun, H. Wang, J. Liang, H. Li, *Chem. Commun.* **2018**, *54*, 4057.
- [4] a) X. Lin, Q. Sun, K. D. Davis, R. Li, X. Sun, *Carbon Energy* **2019**, *1*, 141; b) W. Luo, C.-F. Lin, O. Zhao, M. Noked, Y. Zhang, G. W. Rubloff, L. Hu, *Adv. Energy Mater.* **2017**, *7*, 1601526; c) F. Shen, W. Luo, J. Dai, Y. Yao, M. Zhu, E. Hitz, Y. Tang, Y. Chen, V. L. Sprenkle, X. Li, L. Hu, *Adv. Energy Mater.* **2016**, *6*, 1600377.
- [5] a) Y. Zhao, X. Yang, L. Y. Kuo, P. Kaghazchi, Q. Sun, J. Liang, B. Wang, A. Lushington, R. Li, H. Zhang, X. Sun, *Small* **2018**, *14*, 1703717; b) Y. Zhao, K. R. Adair, X. Sun, *Energy Environ. Sci.* **2018**, *11*, 2673; c) X. Zheng, C. Bommier, W. Luo, L. Jiang, Y. Hao, Y. Huang, *Energy Storage Mater.* **2019**, *16*, 6.
- [6] a) B. Lee, E. Paek, D. Mitlin, S. W. Lee, *Chem. Rev.* **2019**, *119*, 5416; b) W. Luo, Y. Zhang, S. Xu, J. Dai, E. Hitz, Y. Li, C. Yang, C. Chen, B. Liu, L. Hu, *Nano Lett.* **2017**, *17*, 3792; c) H. Wang, C. Wang, E. Matios, W. Li, *Nano Lett.* **2017**, *17*, 6808; d) S. Zhao, B. Qin, K.-Y. Chan, C.-Y. V. Li, F. Li, *Batteries Supercaps* **2019**, *2*, 725; e) B. Sun, P. Xiong, U. Maitra, D. Langsdorf, K. Yan, C. Wang, J. Janek, D. Schröder, G. Wang, *Adv. Mater.* **2020**, *32*, 1903891.
- [7] a) A. Wang, X. Hu, H. Tang, C. Zhang, S. Liu, Y.-W. Yang, Q.-H. Yang, J. Luo, *Angew. Chem.* **2017**, *129*, 12083; b) X. Lin, Q. Sun, H. Yadegari, X. Yang, Y. Zhao, C. Wang, J. Liang, A. Koo, R. Li, X. Sun, *Adv. Funct. Mater.* **2018**, *28*, 1801904; c) B. Sun, P. Li, J. Zhang, D. Wang, P. Munroe, C. Wang, P. H. L. Notten, G. Wang, *Adv. Mater.* **2018**, *30*, 1801334.
- [8] a) Y. Zhao, J. Liang, Q. Sun, L. V. Goncharova, J. Wang, C. Wang, K. R. Adair, X. Li, F. Zhao, Y. Sun, R. Li, X. Sun, *J. Mater. Chem. A* **2019**, *7*, 4119; b) S. Wu, Y. Qiao, K. Jiang, Y. He, S. Guo, H. Zhou, *Adv. Funct. Mater.* **2018**, *28*, 1706374; c) Y.-J. Kim, H. Lee, H. Noh, J. Lee, S. Kim, M.-H. Ryou, Y. M. Lee, H.-T. Kim, *ACS Appl. Mater. Interfaces* **2017**, *9*, 6000.
- [9] a) Y. Zhao, L. V. Goncharova, Q. Zhang, P. Kaghazchi, Q. Sun, A. Lushington, B. Wang, R. Li, X. Sun, *Nano Lett.* **2017**, *17*, 5653; b) Z. Hou, W. Wang, Y. Yu, X. Zhao, Q. Chen, L. Zhao, Q. Di, H. Ju, Z. Quan, *Energy Storage Mater.* **2020**, *24*, 588.
- [10] a) N. Zhao, X. Guo, *J. Phys. Chem. C* **2015**, *119*, 25319; b) J. Kim, H.-D. Lim, H. Gwon, K. Kang, *Phys. Chem. Chem. Phys.* **2013**, *15*, 3623; c) Q. Sun, X. Lin, H. Yadegari, W. Xiao, Y. Zhao, K. R. Adair, R. Li, X. Sun, *J. Mater. Chem. A* **2018**, *6*, 1473; d) Z. E. M. Reeve, C. J. Franko, K. J. Harris, H. Yadegari, X. Sun, G. R. Goward, *J. Am. Chem. Soc.* **2017**, *139*, 595.
- [11] a) C. Liu, M. Carboni, W. R. Brant, R. Pan, J. Hedman, J. Zhu, T. Gustafsson, R. Younesi, *ACS Appl. Mater. Interfaces* **2018**, *10*, 13534; b) X. Bi, X. Ren, Z. Huang, M. Yu, E. Kreidler, Y. Wu, *Chem. Commun.* **2015**, *51*, 7665.
- [12] X. Lin, F. Sun, Q. Sun, S. Wang, J. Luo, C. Zhao, X. Yang, Y. Zhao, C. Wang, R. Li, X. Sun, *Chem. Mater.* **2019**, *31*, 9024.
- [13] B. Sun, C. Pompe, S. Dongmo, J. Zhang, K. Kretschmer, D. Schröder, J. Janek, G. Wang, *Adv. Mater. Technol.* **2018**, *3*, 1800110.
- [14] W. Zhou, Y. Li, S. Xin, J. B. Goodenough, *ACS Cent. Sci.* **2017**, *3*, 52.
- [15] a) J. Kim, H. Park, B. Lee, W. M. Seong, H.-D. Lim, Y. Bae, H. Kim, W. K. Kim, K. H. Ryu, K. Kang, *Nat. Commun.* **2016**, *7*, 10670; b) N. Ortiz-Vitoriano, T. P. Batcho, D. G. Kwabi, B. Han, N. Pour, K. P. C. Yao, C. V. Thompson, Y. Shao-Horn, *J. Phys. Chem. Lett.* **2015**, *6*, 2636; c) H. Yadegari, M. N. Banis, X. Lin, A. Koo, R. Li, X. Sun, *Chem. Mater.* **2018**, *30*, 5156.
- [16] S. Lukas, M. Nika, S. Bettina, W. Martin, S. Christian, S. M. Borisov, S. A. Freunberger, *Angew. Chem., Int. Ed.* **2017**, *56*, 15728.
- [17] a) L. Schafzahl, N. Mahne, B. Schafzahl, M. Wilkening, C. Slugovc, S. M. Borisov, S. A. Freunberger, *Angew. Chem., Int. Ed.* **2017**, *56*, 15728; b) Y. K. Petit, C. Leybold, N. Mahne, E. Mourad, L. Schafzahl, C. Slugovc, S. M. Borisov, S. A. Freunberger, *Angew. Chem., Int. Ed.* **2019**, *58*, 6535.
- [18] Q. Sun, J. Liu, B. Xiao, B. Wang, M. Banis, H. Yadegari, K. R. Adair, R. Li, X. Sun, *Adv. Funct. Mater.* **2019**, *29*, 1808332.